Highest Frequency Detection of FRB 121102 at 4–8 GHz Using the Breakthrough Listen Digital Backend at the Green Bank Telescope

V. Gajjar[1] , A. P. V. Siemion[2,3,4,5], D. C. Price[2,6] , C. J. Law[2,7], D. Michilli[8,9], J. W. T. Hessels[8,9] , S. Chatterjee[10] ,
A. M. Archibald[8,9] , G. C. Bower[11] , C. Brinkman[12], S. Burke-Spolaor[13,14] , J. M. Cordes[10] , S. Croft[2] ,
J. Emilio Enriquez[2,3] , G. Foster[2,15], N. Gizani[2,16], G. Hellbourg[2], H. Isaacson[2] , V. M. Kaspi[17] , T. J. W. Lazio[18],
M. Lebofsky[2], R. S. Lynch[14,19], D. MacMahon[2], M. A. McLaughlin[13,14], S. M. Ransom[20], P. Scholz[21] , A. Seymour[19,22],
L. G. Spitler[23] , S. P. Tendulkar[17] , D. Werthimer[1,2], and Y. G. Zhang[2]

[1] Space Sciences Laboratory, 7 Gauss way, University of California, Berkeley, CA 94720, USA
[2] Department of Astronomy, University of California, Berkeley, 501 Campbell Hall #3411, Berkeley, CA, 94720, USA
[3] Radboud University, Nijmegen, Comeniuslaan 4, 6525 HP Nijmegen, The Netherlands
[4] SETI Institute, Mountain View, California, USA
[5] Institute of Space Sciences and Astronomy, University Of Malta, Malta
[6] Centre for Astrophysics & Supercomputing, Swinburne University of Technology, Hawthorn, VIC 3122, Australia
[7] Radio Astronomy Lab, University of California, Berkeley, CA, 94720, USA
[8] ASTRON, Netherlands Institute for Radio Astronomy, Postbus 2, 7990 AA, Dwingeloo, The Netherlands
[9] Anton Pannekoek Institute for Astronomy, University of Amsterdam, Science Park 904, 1098 XH Amsterdam, The Netherlands
[10] Cornell Center for Astrophysics and Planetary Science and Department of Astronomy, Cornell University, Ithaca, NY 14853, USA
[11] Academia Sinica Institute of Astronomy and Astrophysics, 645 N. A'ohoku Place, Hilo, HI 96720, USA
[12] Physics Department, University of Vermont, Burlington, VT 05401, USA
[13] Department of Physics and Astronomy, West Virginia University, Morgantown, WV 26506, USA
[14] Center for Gravitational Waves and Cosmology, Chestnut Ridge Research Building, Morgantown, WV 26505, USA
[15] University of Oxford, Sub-Department of Astrophysics, Denys Wilkinson Building, Keble Road, Oxford, OX1 3RH, UK
[16] Hellenic Open University, School of Science and Technology, Parodos Aristotelous 18, 26 335 Patra, Greece
[17] Department of Physics and McGill Space Institute, McGill University, 3600 University, Montréal, QC H3A 2T8, Canada
[18] Jet Propulsion Laboratory, California Institute of Technology, Pasadena, CA 91109, USA
[19] Green Bank Observatory, P.O. Box 2, Green Bank, WV 24944, USA
[20] National Radio Astronomy Observatory, Charlottesville, VA 22903, USA
[21] National Research Council of Canada, Herzberg Astronomy and Astrophysics, Dominion Radio Astrophysical Observatory,
P.O. Box 248, Penticton, BC V2A 6J9, Canada
[22] National Astronomy and Ionosphere Center, Arecibo Observatory, PR 00612, USA
[23] Max-Planck-Institut für Radioastronomie, Auf dem Hügel 69, D-53121 Bonn, Germany

Abstract

We report the first detections of the repeating fast radio burst source FRB 121102 above 5.2 GHz. Observations were performed using the 4–8 GHz receiver of the Robert C. Byrd Green Bank Telescope with the Breakthrough Listen digital backend. We present the spectral, temporal, and polarization properties of 21 bursts detected within the first 60 minutes of a total of 6 hr of observations. These observations comprise the highest burst density yet reported in the literature, with 18 bursts being detected in the first 30 minutes. A few bursts clearly show temporal sub-structure with distinct spectral properties. These sub-structures superimpose to provide an enhanced peak signal-to-noise ratio at higher trial dispersion measures. Broad features occur in ~1 GHz wide subbands that typically differ in peak frequency between bursts within the band. Finer-scale structures (~10–50 MHz) within these bursts are consistent with the structure expected from Galactic diffractive interstellar scintillation. The bursts exhibit nearly 100% linear polarization, and a large average rotation measure of $9.359 \pm 0.012 \times 10^4$ rad m^{-2} (in the observer's frame). No circular polarization was found for any burst. We measure an approximately constant polarization position angle in the 13 brightest bursts. The peak flux densities of the reported bursts have average values $(0.2 \pm 0.1$ Jy$)$ similar to those seen at lower frequencies (<3 GHz), while the average burst widths $(0.64 \pm 0.46$ ms$)$ are relatively narrower.

Key words: radio continuum: stars – stars: neutron – supernovae: general

1. Introduction

Fast radio bursts (FRBs) are a class of radio transients with an inferred extragalactic origin due to their anomalously high dispersion measures (DMs) relative to the contribution expected from the Galactic electron distribution (Lorimer et al. 2007). This inference was proven for one source, FRB 121102, when repeated bursts at the DM of 557 pc cm^{-3} were localized by interferometry to be unambiguously associated with a dwarf galaxy at redshift $z = 0.193$ (Chatterjee et al. 2017; Marcote et al. 2017; Tendulkar et al. 2017). Bursts from FRB 121102 have isotropic apparent

radio energies of 10^{40} erg, several orders of magnitude higher than those for any other radio transient on millisecond timescales (Law et al. 2017).

FRB 121102 is the only FRB known to repeat and for which a position is known to sub-arcsecond precision. This has facilitated extensive follow-up observational campaigns. While the burst cadence is irregular, there appear to be epochs in which the source is more active and multiple bursts are detected. For example, Scholz et al. (2016) reported 6 bursts within a 10 minute interval, while several other long observing sessions resulted in non-detections (e.g., Price et al. 2018).

These bursts have so far only been detected between 1 and 5.2 GHz (Scholz et al. 2016; Spitler et al. 2016, 2018; Law et al. 2017; Michilli et al. 2018). Additionally, Law et al. (2017) reported the non-detection of bursts at 70 MHz, 4.5 GHz, and 15 GHz, during epochs in which bursts were detected at 1.4 and 3 GHz, indicating that some bursts are not likely to be broadband.

Propagation effects, such as scintillation and plasma lensing, can significantly alter the observed radio emission from impulsive radio sources (Macquart & Johnston 2015; Cordes et al. 2017). Estimates of the FRB burst rate have taken into account the observed bursts (e.g., Lawrence et al. 2017); however, the observed radio emission could be affected by these propagation effects. Disentangling the intrinsic emission from propagation effects is thus an important goal in FRB science. Detection of bursts at different frequencies and over wider bandwidths is helpful for studying the frequency dependence of potential propagation effects. Measurement of burst polarization can also shed light on emission physics and the source's local environment. Recently, Michilli et al. (2018) reported a very high and variable Faraday rotation measure (RM) of $\sim 10^5$ rad m^{-2} for FRB 121102, suggesting that this source is embedded in an extreme and dynamic magnetoionic environment.

Here, we report the detection of 21 bursts from FRB 121102 —all of which occurred within an hour—using the 4–8 GHz receiver on the Robert C. Byrd Green Bank Telescope (GBT) and the Breakthrough Listen (BL) backend. It should be noted that 15 of these detections were announced briefly in Gajjar et al. (2017). Here, we are providing a more detailed analysis. These are the highest-frequency detections of bursts from any FRB to date.

This paper is structured as follows. In Section 2, we describe our observations. In Section 3.1 we highlight issues with finding a true DM for the bursts, followed by a discussion on the spectrotemporal structures in a subset of bursts in Section 3.2. We confirm and extend the results of Michilli et al. (2018) by performing polarimetry on baseband voltage data in Section 3.3. Our wide instantaneous bandwidth reveals these bursts to be confined to a fraction of the 4–8 GHz band, with dynamic structure varying on short timescales, which are further discussed in Section 3.4. A brief discussion of our findings is in Section 4 and a summary is provided in Section 5.

2. Observations

Observations of FRB 121102 were conducted with the GBT as part of the BL project (Worden et al. 2017). BL is a comprehensive search for extraterrestrial intelligence (SETI) employing both optical and radio telescopes; the BL target list includes nearby stars and nearby galaxies, as well as other anomalous astronomical sources broadly classified as "exotica" (Isaacson et al. 2017). As a component of the latter category, BL is conducting a targeted SETI effort toward known FRB positions to investigate any associated artificial signals and/or underlying modulation pattern, hypothesizing that one or more FRBs may be deliberate artificial beacons or other manifestations of technology (e.g., Lingam & Loeb 2017).[24]

Observations using the 4–8 GHz (C-band) receiver on the GBT were conducted on 2017 August 26 during a 6 hr BL

observing block. The initial hour (with scans numbered from 0 to 10) was used to configure various telescope settings and calibration procedures. The calibrator 3C 161 and an off-source position were observed for one minute each, along with a calibration noise diode, and used for flux and polarization calibration using the `pac` tool in PSRCHIVE. A 5-minute observation of the bright pulsar PSR B0329+54 was also performed as a diagnostic to verify polarization and flux density measurements. The remaining five hours of the session were divided into ten 30 minute scans of FRB 121102, identified with scan numbers ranging from 11 to 20.

Observations were conducted with the BL digital backend (MacMahon et al. 2018), which recorded 8-bit baseband voltage data across the entire 4 GHz receiver bandwidth. The GBT analog downconversion system provided four 1500 MHz wide tunable passbands to cover the 4–8 GHz band, configured with central on-sky frequencies of 4625.0, 5937.5, 7250.0, and 8562.5 MHz. These frequencies were chosen such that the signal at the edges of each passband's intermediate frequency filter overlapped the adjacent passband by 187.5 MHz.

Each dual-polarization passband was Nyquist-sampled using 8-bit digitizers, polyphase channelized to 512 "coarse" frequency channels, requantized to 8 bits, and then distributed to a cluster of compute nodes that recorded these data to disk. Directly after observations, the coarsely channelized voltage data were further channelized (to 366 kHz resolution), integrated (with a sampling time of 350 μs) using a custom GPU-accelerated spectroscopy code, and finally written onto SIGPROC[25] filterbank files as total intensity (Stokes *I*) dynamic spectra with 4096 spectral channels.

These dynamic spectra were searched using the Heimdall package (Barsdell et al. 2012) for dispersed pulses within the DM range of 500–700 pc cm^{-3}, using a DM interval of 0.1 pc cm^{-3}. We detected 21 bursts above a threshold signal-to-noise ratio (S/N) of six. A section of raw voltages (of total 1.5 s) around each detected burst was extracted for further processing and coherently dedispersed to a DM of 565.0 pc cm^{-3} (see Section 3.1) using the DSPSR package (van Straten & Bailes 2011). The coherently dedispersed PSRFITS data products have temporal and spectral resolutions of 10.1 μs and 183 kHz, respectively.[26] We have discarded the lowest part of the frequency band (4–4.5 GHz) in further analyses due to spurious radio frequency interference.

3. Analysis

PSRCHIVE (van Straten et al. 2012) and custom Python scripts were used to measure the properties of the detected bursts. Table 1 lists various parameters determined for each burst. Among the 10 recorded scans, all reported detections occurred in the first hour, i.e., from scans 11 and 12. We assigned the bursts identifiers 11A through 11R, and 12A through 12C, according to their scan number and order of arrival.

3.1. DM Optimization

The DM of FRB 121102 has been previously reported to range between 553 and 569 pc cm^{-3} (Spitler et al. 2014, 2016; Scholz et al. 2016; Law et al. 2017) from lower-frequency

---

[24] However, we emphasize here that it is unlikely that the bursts we detected were transmitted from an intelligent civilization.

Table 1
Properties of All 21 Bursts

Pulse	MJD (57991+)	S/N	$DM_{S/N}$ (pc cm^{-3})	S_{peak} (mJy)	Width (ms)	F(Jy ms)	RM_{obs} (rad m^{-2})	PA_{∞}^{mean} (degree)	ΔPA_{∞} (degree)
11A	0.409904044	55.7	601 ± 18	380.5	1.74 ± 0.01	0.62	93559 ± 18	63.9 ± 0.4	6
11B	0.412764720	7.1	585 ± 15	51.9	0.39 ± 0.16	0.02	...	...	...
11C	0.413019871	9.9	574 ± 15	85.2	0.42 ± 0.08	0.03	...	...	...
11D	0.413458764	37.0	583 ± 33	314.8	0.68 ± 0.08	0.23	93503 ± 53	79.2 ± 0.3	4
11E	0.413706653	28.2	591 ± 18	126.8	1.15 ± 0.08	0.14	93577 ± 43	80.9 ± 0.8	6
11F	0.413837058	29.2	588 ± 49	157.5	0.92 ± 0.08	0.13	93836 ± 160	86.5 ± 0.7	5
11G	0.416436793	7.6	574 ± 10	52.9	0.31 ± 0.08	0.02	...	...	...
11H	0.416633362	58.0	575 ± 33	699.9	0.27 ± 0.01	0.18	93467 ± 35	76.4 ± 0.3	8
11I	0.417714722	13.4	569 ± 10	125.5	0.34 ± 0.08	0.04	93648 ± 59	77.2 ± 1.2	4
11J	0.417865553	9.9	573 ± 19	118.6	0.39 ± 0.08	0.04	...	...	...
11K	0.418627200	13.9	591 ± 32	105.2	0.81 ± 0.08	0.06	93567 ± 248	77.9 ± 1.3	5
11L	0.419449885	8.4	598 ± 19	...	<0.70	...	...	...	...
11M	0.421212904	11.1	566 ± 20	94.7	0.41 ± 0.08	0.04	...	...	...
11N	0.421712667	12.4	565 ± 6	256.7	0.19 ± 0.01	0.04	93513 ± 60	81.8 ± 0.8	5
11O	0.422939456	12.1	584 ± 14	139.9	0.41 ± 0.08	0.04	93802 ± 224	76.9 ± 1.2	2
11P	0.424270656	6.4	601 ± 31	...	<1.79	...	...	...	
11Q	0.426552515	20.9	562 ± 23	400.2	0.18 ± 0.01	0.07	93502 ± 62	79.5 ± 0.4	5
11R	0.430427904	7.4	568 ± 15	...	<0.27	...	...	...	...
12A	0.431974007	13.6	572 ± 56	132.2	0.72 ± 0.08	0.07	93452 ± 111	80.4 ± 0.4	5
12B	0.439360677	20.6	636 ± 11	331.4	1.68 ± 0.01	0.45	93643 ± 62	61.8 ± 0.6	7
12C	0.448427650	10.7	580 ± 40	118.8	0.68 ± 0.08	0.07	93593 ± 101	73.5 ± 0.7	11

Note. The columns list, from left to right: burst numbers, barycentric arrival time at infinite frequency, S/N, the DM that maximizes S/N, peak flux density, the width of the burst, fluence, RM (in the observer's frame), the weighted average PA at infinite frequency, and the standard deviation of PA across the pulse phase, respectively. We were not able to flux-calibrate bursts 11L, 11P, and 11R due to low S/N. Also, for these pulses we sub-integrated adjacent time bins and hence could only obtain an upper limits on the widths.

observations. For each burst detected here, we measured the S/N as a function of DM, and found that individual bursts show slightly different peak S/N-maximizing DMs. These S/Ns correspond to the peak flux densities obtained after integrating the entire 4.5–8 GHz band. For bursts 11B, 11L, 11M, and 11R, which are confined to a limited fraction of the entire band, we have used only that portion of the band to better estimate S/N-maximizing DM uncertainties. Estimated S/N-maximizing DMs for all 21 bursts are listed in Table 1. To investigate further, we coherently dedispersed raw voltages from burst 11A across a range of DMs with a DM step of 5 pc cm^{-3}. This investigation led to the discovery of detailed spectrotemporal structures (*components*, see Figure 1 and Section 3.2). It is likely that the differences between the DMs originate from how these components superimpose for different trial values of DM. Figure 1 shows burst 11A dedispersed and detected at three different DMs. While it is not clear if these components are intrinsic to the emission mechanism or due to propagation effects, their peculiar alignment provides enhanced S/N at higher DMs compared to previously reported DMs (Spitler et al. 2014, 2016; Scholz et al. 2016; Law et al. 2017).

Assuming these components to be intrinsic, we optimized the S/Ns of individual components by maximizing the average absolute rate of change of the total flux density, which we call here a *structure parameter*, across the pulse window defined as,

$$\text{Structure Parameter} = \frac{1}{n} \sum_{i}^{n} \left| \frac{S_i - S_{i+1}}{\Delta t} \right|. \quad (1)$$

Here, n is the number of on-pulse bins, S_i is the flux at the ith bin, and Δt is the time resolution. This structure-parameter-maximizing DM differs significantly from the S/N-maximizing DM (see Figure 1). Similar techniques have also been explored and will be reported in detail in J. W. Hessels et al. (2018, in

preparation) at lower frequencies. Although an analysis of this type was not possible for most of our detected pulses due to either low S/N, fewer components, or both, we assumed a structure-maximizing DM of 565.0 pc cm^{-3} to be consistent for all our bursts and used that value in coherent dedispersion. We note that this estimate can be off by our DM resolution in Figure 1 from a "true" DM (i.e., ±5 pc cm^{-3}).

3.2. Spectrotemporal Components

We found highly variable temporal and spectral features in many of the bursts. Figure 2 shows dynamic spectra of all bursts after coherent dedispersion at a DM of 565 pc cm^{-3}. Bursts 11A and 12B exhibit distinct components, while bursts such as 11E, 11K, and 11O show some indication of unresolved components. For bursts 11D and 11F, such components are not clearly visible but likely give rise to the slanted or curved features seen in the dynamic spectra. Each burst was modeled as a sum of multiple Gaussian components using the PSRCHIVE utility pass. The model was then used to derive average widths and fluences for all bursts (see Table 1). We note that the burst widths found here are relatively narrow compared to the burst widths seen at lower frequencies (<3 GHz)—as also noted for the Arecibo sample of 4.5 GHz bursts presented by Michilli et al. (2018).

Bursts 11A and 12B clearly exhibit distinct components. The overall shape of burst 11A is strikingly similar to micro-structures seen for FRB 170827 at lower frequencies (Farah et al. 2018). We identify four components in burst 11A integrated across 4.5–8 GHz, with individual widths of 0.18, 0.10, 0.25, and 0.51 ms. from the leading component to the trailing component, respectively. For the fourth component, it was evident that a single Gaussian function did not represent its true shape, thus, we used a hybrid function, which is
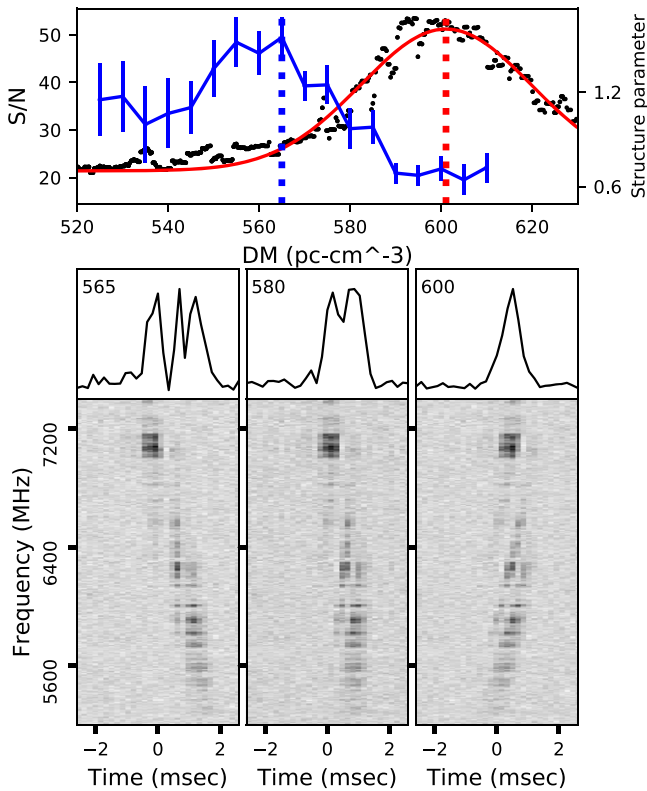
Figure 1. DM analysis for burst 11A. The top panel shows the S/N (black) and structure parameter (blue) as a function of DM. The black points are S/N measurements and the red line is a best-fit model of a Gaussian function. The blue points are measured structure parameter values with corresponding errors. The red and blue dotted lines are for S/N- and structure-maximizing DMs, respectively. The bottom three panels show dynamic spectra, along with average pulse profiles at three different trial DMs, labeled in the top left corners. At the highest trial DM of 600 pc cm^{-3}, the alignment of burst structures produces the highest S/N, while at the trial DM of 565 pc cm^{-3} these structures appear to be well separated.

combination of a Gaussian and an exponential decay function, to estimate its width. It should be noted that this is just a mathematical representation of the shape and we are not inferring an exponential function as a scattering tail. These components show varying spectral extents, with the first two limited to higher frequencies and the last two at lower frequencies. Additionally, components three and four show a very sharp rise and gradual decay of the burst energy. Component four exhibits a gradual increase in burst width toward lower frequencies. To compare the width of the fourth component across the observed band, we extracted dynamic spectra with widths of 200 MHz centered around 6200, 5980, 5780, and 5460 MHz. An integrated profile of the fourth component at these frequencies was found to have widths of 0.22, 0.24, 0.34 and 0.41 ms, respectively. More detailed analyses of the progressive drift in pulse profile components, as seen at other radio frequency bands, are presented in J. W. Hessels et al. (2018, in preparation).

Burst 12B also exhibits two resolved components with widths of 0.29 and 0.30 ms, separated by ∼2 ms. As with 11A, the leading component spans higher frequencies, while the trailing component spans lower frequencies. In contrast to 11A, the trailing component of 12B does not show an increase in width at lower frequencies. While there may be a third component on the leading edge of the second component, the burst S/N is not sufficient for verification.

3.3. Faraday Rotation

We determined the Faraday RM of the bursts by performing a brute-force search of the linear polarization fraction at different RM trials with the `rmfit` tool from PSRCHIVE. We developed a custom routine to correct for the initial RM values from `rmfit` and fit a quadratic function to the complex angles determined by the Stokes parameters. This technique refines the initial RMs and computes a polarization angle (PA) for each burst. A detailed description of this technique can be found in Michilli et al. (2018). This approach was motivated by the extremely variable spectral properties of the bursts. From the 13 brightest bursts that could be analyzed using this technique, we find a mean RM of 93589 ± 118 rad m^{-2}. The RMs found here differ by 9169 ± 122 rad m^{-2} from the RMs of the bursts detected from Arecibo at 4.5 GHz by Michilli et al. (2018). After de-rotating the Stokes Q and U using the best-fit value of RM, all 13 bursts show a ∼100% linear polarization fraction and uniform PAs across the burst (Figure 2). We have only considered PAs from the phase bins with linear polarization above 3σ. The weighted mean PA for each burst, measured after weights calculated empirically from the variance in PAs across these phase bins, is listed in Table 1. The uncertainty on the weighted PA was measured as a sum of all weights for each burst. It should be noted that the PA is roughly uniform across the pulse phase; however, there are apparently significant variations (∼7°) in the average PA between all observed bursts at the ∼3σ level. For example, bursts 11A and 12B show slightly lower PAs compared to rest of the reported bursts. These differences in PAs could possibly arise from our uncertainties in the RM measurements, as these two quantities are covariant. No circular polarization was found for any burst and any undetected circular polarization is less than a few percent.

3.4. Burst-to-burst Spectral Variation

Figure 3 shows measured flux density as a function of observing frequency and time for the 17 brightest bursts. The peak flux frequency is not constant within the observed frequency band; similar spectral variation between bursts has also been reported by previous studies (Spitler et al. 2016; Law et al. 2017; Scholz et al. 2017; Michilli et al. 2018). These large-scale frequency features are approximately of the order of ∼1 GHz in extent. To estimate the average number of discrete large-scale structures, we divided the spectrum from each burst into multiple bins, each 94 MHz wide, and then calculated the total amount of spectral energy in each bin (Figure 4). The overall spectral energy distribution shows two approximately GHz wide peaks around 6 and 7.2 GHz, with a possible trough in the spectral energy between 6.5 and 7 GHz. It should be noted that this spectral behavior is based on our detections of only 21 bursts. It is possible that the detection of a larger sample of bursts might fill this trough.

Figure 3 shows that bursts exhibit marked differences in their spectral extent and spectral peaks. Some bursts, such as 11A, show emission across the entire observed band; others, such as 11C, 11H and 11K, show emission only at the highest frequencies. Bursts 11G, 11N, and 12A show a concentration of emission in the lower half of the band. Bursts 11A to 11F exhibit a spectral peak around 7 GHz, which appears to then shift to lower frequencies in later bursts.
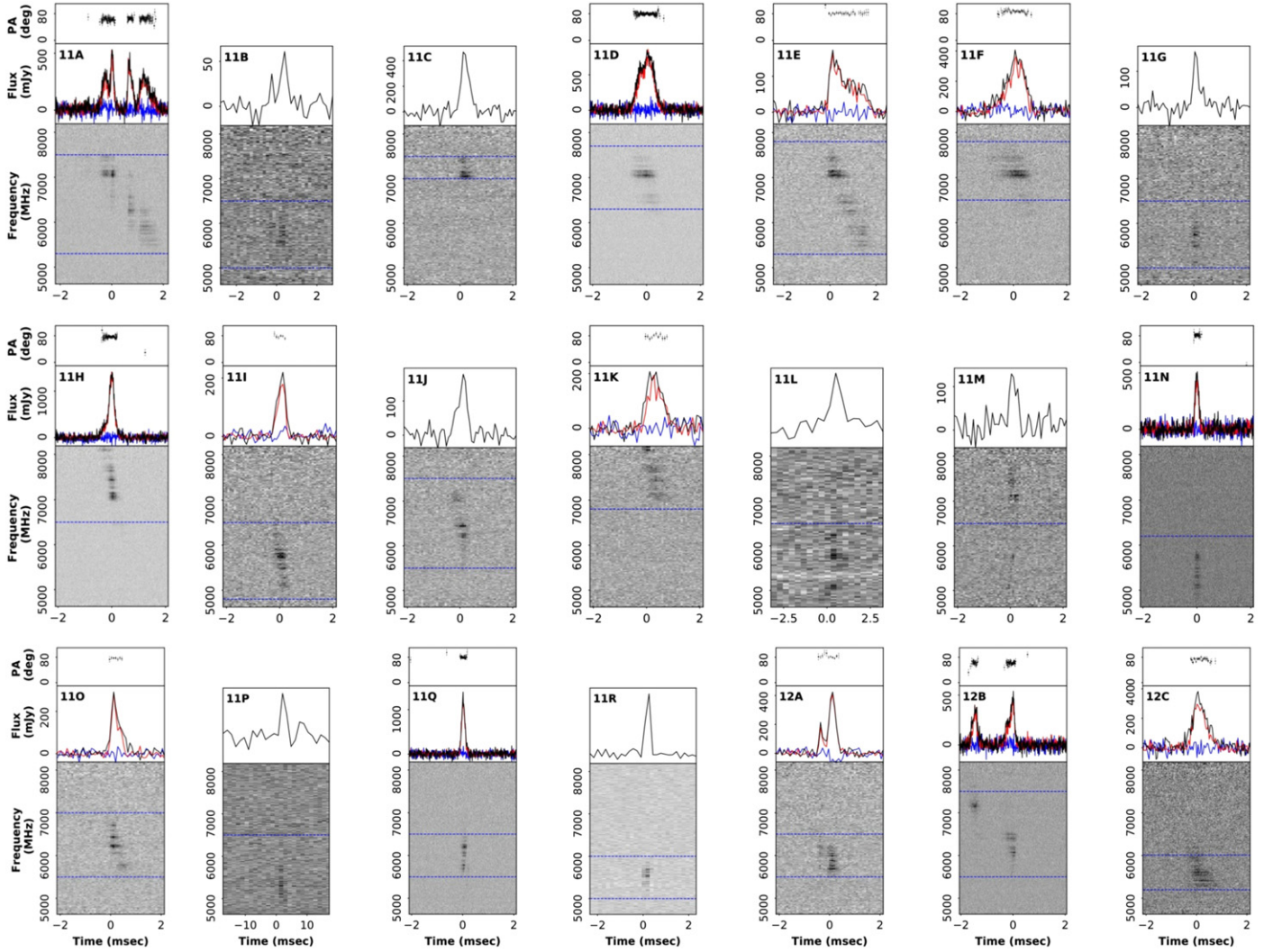
Figure 2. Dynamic spectra of all 21 detected bursts, coherently dedispersed at the DM of 565 pc cm^{-3}. The waterfall data are frequency (*Y*-axis) vs. time (*X*-axis) with units of MHz and ms, respectively, with intensity indicated on a linear scale. The grayscales are different and scaled according to individual pulse S/Ns. The top panels show flux density (mJy), and for 12 bursts show circular (blue) and linear (red) polarization and position angle (PA), referenced to infinite frequency. The dashed horizontal blue lines are frequency boundaries, as the profile for each burst was obtained after adding frequencies between these boundaries to enhance S/N.

In order to assess the origin of large- and finer-scale frequency structures seen in Figures 2 and 3, we calculated the Galactic scintillation bandwidth across the observed band. We used the NE2001 model (Cordes & Lazio 2002), and estimated a Galactic scattering timescale $\tau_s = 20\,\mu\text{s}\,\nu^{-\alpha}$ toward the direction of FRB 121102 (ν is the observing frequency in GHz, while α is the scaling parameter). Assuming a frequency scaling for a Kolmogorov spectrum with scaling parameter, x, between 4 and 4.4 (Cordes & Lazio 2002; Bhat et al. 2004), we estimate the expected diffractive interstellar scintillation bandwidth as (Lambert & Rickett 1999)

$$\Delta f_{\text{DISS}} = \frac{1.16}{2\pi\tau_s} = \frac{1.16\nu^x}{40\pi}\ \text{MHz}. \qquad (2)$$

For the observed band (4.5–8 GHz), the predicted Δf_{DISS} varies from 7 to 87 MHz (assuming a scaling parameter of 4.4). Thus, the large-scale frequency structures (~GHz wide) are likely to be intrinsic to the source and/or due to propagation effects in the source's local environment.

To compare these predicted values for Δf_{DISS} with fine-scale frequency structures from the detected bursts, we obtained

spectra for each burst by selecting an appropriate on-pulse window. Following the procedure of Cordes et al. (1985) and Cordes (1986), we then computed auto-correlation functions (ACFs) for these spectra (Figure 5). As the spectral extent of a few bursts were significantly broad—spanning over 3 GHz—the ACFs over the entire spectra produce a multi-featured ACF with multiple widths. To measure the characteristic bandwidth for a given burst, we divided each spectrum into two or three parts, depending upon the spectral extent. We then fitted a Gaussian function to the ACF to obtain the half width at half maximum as a characteristic bandwidth for the given sub-spectra for each burst.

We found that the ACFs showed different characteristic bandwidths in different sub-spectra in the 4.5–8 GHz band. Table 2 shows these characteristic bandwidths from 15 stronger bursts. The measured characteristic bandwidth follows the expected Δf_{DISS} across the 4.5–8 GHz band (see Figure 6), suggesting that the fine-scale frequency structures seen in each of these bursts are likely due to Galactic interstellar scintillation, with a few exceptions. For example, burst 11H does not appear to show characteristic bandwidth matching with the
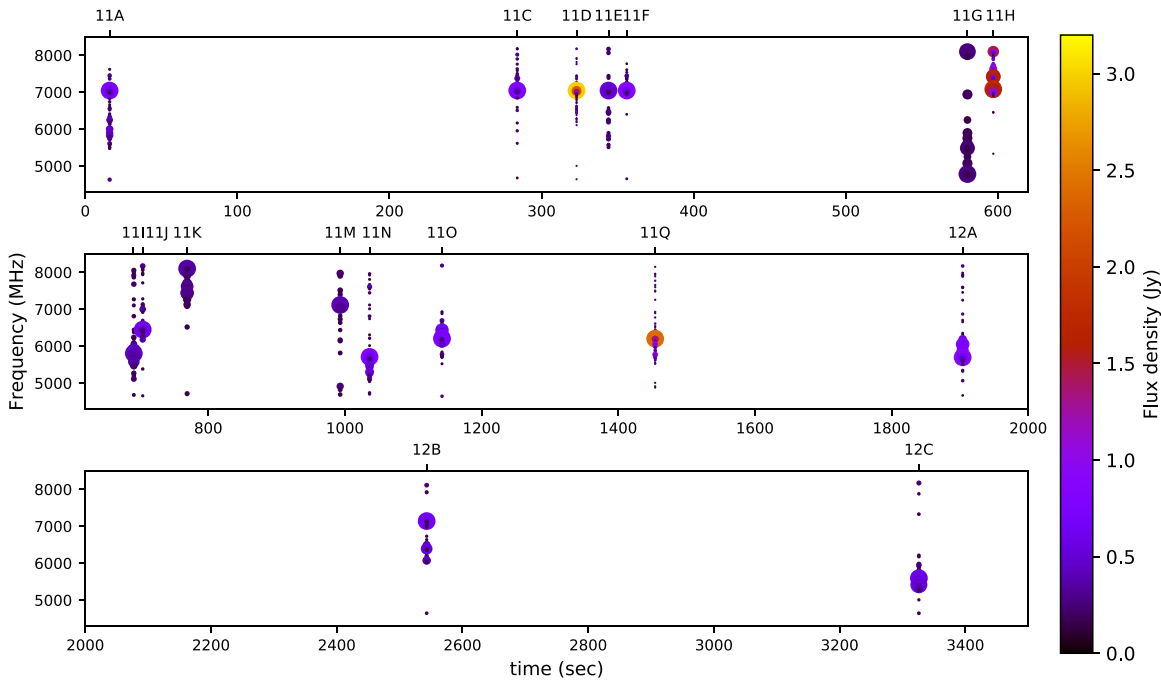
Figure 3. Burst-to-burst spectral properties as a function of time for the FRB 121102 bursts presented here. Panels (top to bottom) show spectra for each burst at their corresponding arrival times for 17 bright bursts detected during the first observing hour. Each spectrum is shown with 11 MHz of spectral resolution to highlight large-scale frequency structures and rapid variation of spectral peaks. The color represents absolute flux density across all bursts, while the circle size represents flux density relative to the peak flux density for a given burst on a base-2 logarithmic scale.
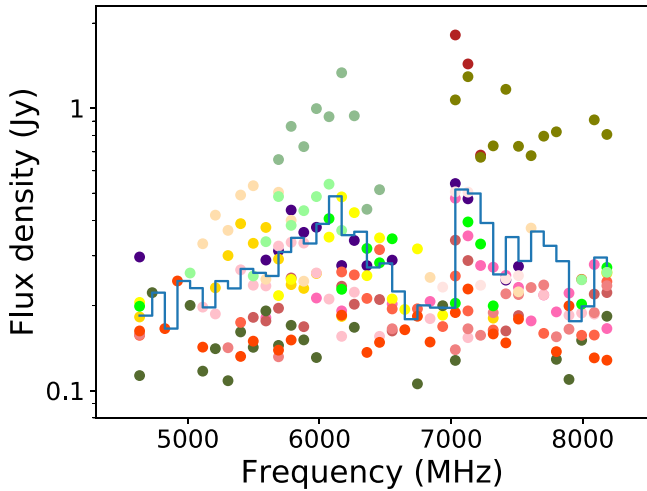

Figure 4. Average spectral energy distribution of FRB 121102 bursts presented here. Different colors represent histograms of spectral energy for different bursts, binned with a resolution of 94 MHz. The blue line represents the mean. Most bursts show spectral peaks near 6 GHz or 7.2 GHz and an apparent trough between 6.5 and 7 GHz.

Δf_{DISS} at higher frequencies. However, this could be a statistical fluctuation, given the small number of scintiles in the burst.

4. Discussion

4.1. Instantaneous Burst Rate

Our detection of 21 bursts within 60 minutes represents the highest number of bursts detected within a short interval (i.e., hour timescale), with 18 bursts occurring in the first 30 minutes. We did not detect any bursts during the following 4 hr of observations, which supports the idea that FRB 121102's bursting behavior is episodic. This could be due to intrinsic changes in the emission conditions or due to more favorable "plasma lensing" conditions (Cordes et al. 2017) during the first hour, potentially enhancing observed burst energies by an order of magnitude.

Our observations highlight the advantages afforded by wider instantaneous bandwidth. If our 4 GHz instantaneous bandwidths were halved, we would only have detected 10–12 bursts, mainly as the band-limited spectral structures they exhibit would have fallen out of the band (Figure 2). Law et al. (2017) have also pointed out similar limitations of narrow bandwidth observations.

The spectral peak variation of each burst and apparent band-limited characteristics indicate that further bursts may be detected by searching for pulses over subbands, particularly in observations over large fractional bandwidths. The existence of spectral structure may also impact the performance of single-pulse search pipelines, which are generally designed to search for broadband pulses.

4.2. Average Spectral and Temporal Properties across 1–8 GHz

We compared the average peak flux densities of all our bursts with previously reported observations at various lower frequencies, as shown in Figure 7(a). We found that statistically the distribution of peak flux densities across frequency is consistent with being flat across 1–8 GHz. It should be noted that these measurements were obtained from different telescopes at very different epochs, which might affect their intrinsic absolute scaling. The different sensitivities of different telescopes at various frequencies are also highlighted in Figure 7(a). We also compared the burst widths at various frequencies (Figure 7(b)) and highlight that bursts are relatively narrower at higher frequencies (>4 GHz).
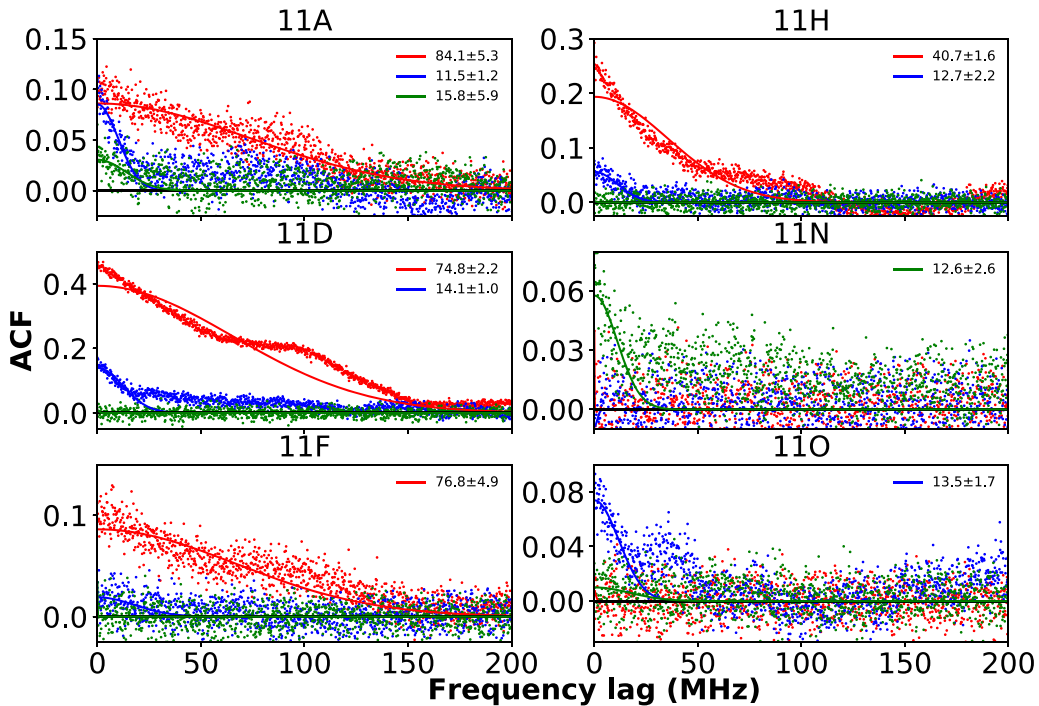
Figure 5. Example ACFs from different subbands of the entire 4.5–8 GHz bandwidth for six of the FRB 121102 bursts presented here. The red, blue, and green dots with fitted Gaussian functions are from sub-spectra centered at frequencies of 7500, 6500, and 5200 MHz, respectively. The characteristic bandwidths (in MHz) for each subband are shown as inset text with corresponding errors (1σ).

The apparently flat spectrum of FRB 121102 stands in contrast to the steep spectral indices observed for most neutron star emission. Giant pulses (GPs) from the Crab pulsar, for instance, typically exhibit a very steep spectrum with a power-law index $\alpha = -2.6$ and a steep power-law distribution of rates at a fixed fluence (Meyers et al. 2017). Ordinary pulsars also show very steep spectra, with a mean index $\alpha = -1.4$ (Bates et al. 2013). An important exception is the radio to millimeter spectrum of magnetars. The Galactic Center magnetar, SGR J1745−2900, has been observed to have a flat spectrum up to 291 GHz (Torne et al. 2017). The similarity in spectral index between FRB 121102 and radio magnetars suggests a common emission mechanism. It is likely that further high-frequency observations with better sensitivity, enabling the detection of weaker bursts, may provide better constraints on the steepness of the spectral index.

If the apparently flat spectral behavior of FRB 121102 is a common property for other FRBs, we suggest that future FRB surveys could be conducted effectively at higher frequencies, utilizing either a fly's eye mode or multiple beams to compensate for a smaller field of view. Higher-frequency observations may also have lower terrestrial radio interference and larger instantaneous receiver bandwidths—potentially beneficial for detecting more of these spectrally limited bursts. Similar suggestions were also made by Law et al. (2017).

4.3. Frequency Structures

The large-scale frequency structures are unlikely to be instrumental in nature and are likely intrinsic to the progenitor or propagation effects imparted in the source's local environment. We note the similarity of these structures to the banded structures seen for the Crab GPs at similar high radio frequencies reported by Hankins & Eilek (2007) and Jones (2010). We also found that burst-to-burst large-scale spectral

properties change on the order of tens of seconds. If bursts from FRB 121102 have a physical origin similar to Crab GPs, then such changes are comparable to similar spectral feature variations between Crab GPs, although these manifest at a shorter timescale (few microseconds). The fine-scale structures appear to be due to the Galactic DISS. This is consistent with the angular diameter of the bursts measured at 1.7 GHz from VLBI (Marcote et al. 2017).

4.4. High Faraday RM

The high RM found here for FRB 121102 is almost 500 times greater than the RMs reported for any other FRB (e.g., Masui et al. 2015) and somewhat larger than the RM of the Galactic center magnetar SGR J1745−2900 (Eatough et al. 2013). Our measured RM is about 10% lower than the RM from bursts detected at 4–5 GHz, from data obtained seven months prior to the observations reported here. This change in the RM is already highlighted in Michilli et al. (2018). This is a significant change in the RM and further justifies regular monitoring to clarify how the RM varies with time. SGR J1745−2900 also shows changes in the RMs on a similar scale over four years of regular monitoring (Desvignes et al. 2018).

The high RM suggests an intense magnetic field, at least 1 mG, in the progenitor's environment. As noted in Michilli et al. (2018), plausible scenarios that could produce this RM include: the source being in the vicinity of an intermediate-mass or supermassive black hole, like SGR J1745−2900 (Eatough et al. 2013) or inside a powerful pulsar wind nebula, or a supernova remnant. Piro (2016) suggested that an expanding supernova shell could also cause the RM to decrease with time, as reported here. However, such changes can also cause the corresponding DM to decrease with time by a similar factor, which was not observed. Other FRBs might have similarly high RMs; however, measuring large RMs

Table 2
Table of Characteristic Bandwidths for 15 Bursts from FRB 121102
across 4.5 to 8 GHz

Burst	Frequency (GHz)	Δf (MHz)
11A	7.595	84.1 ± 5.3
	6.407	11.5 ± 1.2
	5.220	15.8 ± 5.9
11D	7.595	74.8 ± 2.2
	6.407	14.1 ± 1.0
11E	7.595	73 ± 11
	6.407	19 ± 13
	5.220	13 ± 11
11F	7.595	76.8 ± 4.9
	6.407	20 ± 17
11G	5.220	2.3 ± 2.1
11H	7.595	40.7 ± 1.6
	6.407	12.7 ± 2.2
11I	5.517	15.7 ± 6.0
11J	7.298	59 ± 23
11K	6.407	24 ± 26
11N	5.517	15.2 ± 3.6
11O	6.407	13.5 ± 1.7
11Q	6.407	17.1 ± 1.3
12A	5.517	13.3 ± 1.7
12B	7.595	83 ± 14
	6.407	16.7 ± 3.7
12C	5.517	16.3 ± 2.7

Note. The second column lists the center frequency of the sub-spectra used to calculate the characteristic bandwidths from ACFs listed in the third column with corresponding errors (3σ).
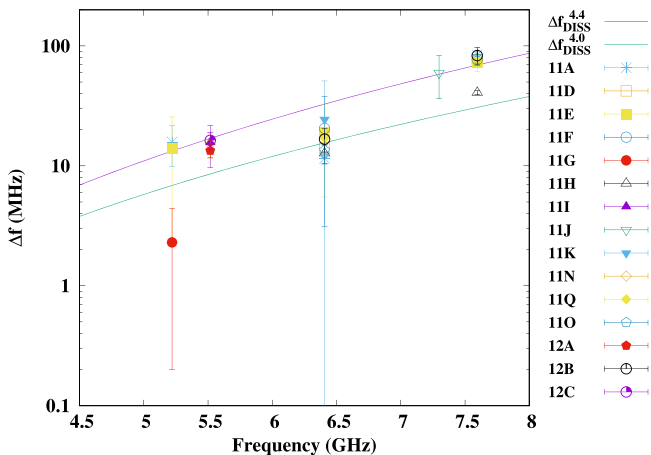

Figure 6. Measured characteristic bandwidths (in MHz) of 15 individual strong bursts, for various subbands, along with the expected Δf_{DISS} (with two different scaling parameters) from Galactic diffractive scintillations (see Equation (2)).

requires higher frequency resolution at lower frequencies (e.g., $\leqslant 3$ GHz) to avoid intra-channel depolarization. For example, to search for RM up to $10^5\,\text{rad}\,\text{m}^{-2}$, the required channel resolution is of the order of tens of kHz at 1 GHz. This again
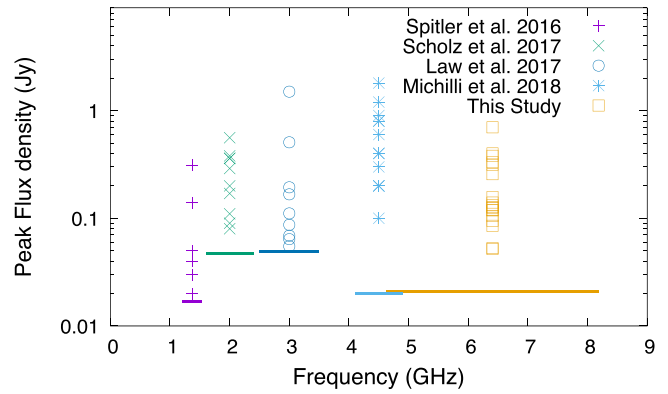
(a)
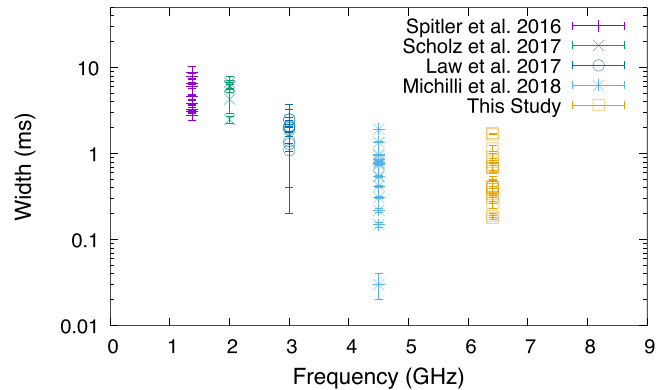
(b)

Figure 7. (a) Average peak flux densities as a function of observed frequency from this and previous studies. The horizontal lines represent the minimum detectable flux density ($\geqslant 6\sigma$) for a 1 ms wide pulse, with a horizontal extent showing the observational frequency bandwidths at different frequencies. (b) Observed burst widths as a function of observed frequency from previous studies, indicating that higher-frequency bursts are relatively narrower.

highlights the utility of high-frequency observations of FRBs, as intra-channel depolarization is inversely proportional to observational frequency to the third power.

5. Conclusion

We have reported, for the first time, that FRB 121102 is active above 5.2 GHz. The 21 bursts detected over 60 minutes represent the highest instantaneous burst rate yet observed. We have confirmed that bursts from FRB 121102 are highly linearly polarized, that the source shows a large RM of $93589 \pm 118\,\text{rad}\,\text{m}^{-2}$, and that the diverse and variable spectral and temporal properties seen at lower frequencies are also exhibited above 5 GHz. As seen at lower frequencies (Scholz et al. 2016; Spitler et al. 2016; Law et al. 2017), we also found that the source exhibits large-scale frequency structures that could be intrinsic, imparted by its local environment. These structures vary between bursts and can bias the estimation of burst properties, such as DM and pulse width, as they superimpose to provide an enhanced S/N at higher trial DMs. We found fine-scale structure consistent with Galactic interstellar scintillation. Future observations of this source will help to answer some of the lingering questions, including whether the source exhibits any periodicity, at what

frequency the apparently flat spectral index transitions, and how the event rate varies as a function of frequency.

ORCID iDs

V. Gajjar ● https://orcid.org/0000-0002-8604-106X
D. C. Price ● https://orcid.org/0000-0003-2783-1608
C. J. Law ● https://orcid.org/0000-0002-4119-9963
J. W. T. Hessels ● https://orcid.org/0000-0003-2317-1446
S. Chatterjee ● https://orcid.org/0000-0002-2878-1502
A. M. Archibald ● https://orcid.org/0000-0003-0638-3340
G. C. Bower ● https://orcid.org/0000-0003-4056-9982
S. Burke-Spolaor ● https://orcid.org/0000-0003-4052-7838
J. M. Cordes ● https://orcid.org/0000-0002-4049-1882
S. Croft ● https://orcid.org/0000-0003-4823-129X
J. Emilio Enriquez ● https://orcid.org/0000-0003-2516-3546
H. Isaacson ● https://orcid.org/0000-0002-0531-1073
V. M. Kaspi ● https://orcid.org/0000-0001-9345-0307
M. A. McLaughlin ● https://orcid.org/0000-0001-7697-7422
S. M. Ransom ● https://orcid.org/0000-0001-5799-9714
P. Scholz ● https://orcid.org/0000-0002-7374-7119
L. G. Spitler ● https://orcid.org/0000-0002-3775-8291
S. P. Tendulkar ● https://orcid.org/0000-0003-2548-2926

References

Barsdell, B. R., Bailes, M., Barnes, D. G., & Fluke, C. J. 2012, MNRAS, 422, 379
Bates, S. D., Lorimer, D. R., & Verbiest, J. P. W. 2013, MNRAS, 431, 1352
Bhat, N. D. R., Cordes, J. M., Camilo, F., Nice, D. J., & Lorimer, D. R. 2004, ApJ, 605, 759
Chatterjee, S., Law, C. J., Wharton, R. S., et al. 2017, Natur, 541, 58
Cordes, J. M. 1986, ApJ, 311, 183
Cordes, J. M., & Lazio, T. J. W. 2002, arXiv:astro-ph/0207156
Cordes, J. M., Wasserman, I., Hessels, J. W. T., et al. 2017, ApJ, 842, 35
Cordes, J. M., Weisberg, J. M., & Boriakoff, V. 1985, ApJ, 288, 221
Desvignes, G., Eatough, R. P., Pen, U. L., et al. 2018, ApJL, 852, L12
Eatough, R. P., Falcke, H., Karuppusamy, R., et al. 2013, Natur, 501, 391
Farah, W., Flynn, C., Bailes, M., et al. 2018, MNRAS, in press, doi:10.1093/mnras/sty1122
Gajjar, V., Siemion, A. P. V., MacMahon, D. H. E., et al. 2017, ATel, 10675
Hankins, T. H., & Eilek, J. A. 2007, ApJ, 670, 693
Isaacson, H., Siemion, A. P. V., Marcy, G. W., et al. 2017, PASA, 129, 054501
Jones, G. E. 2010, PhD thesis, California Inst. Tech., http://resolver.caltech.edu/CaltechTHESIS:10122009-094525715
Lambert, H. C., & Rickett, B. J. 1999, ApJ, 517, 299
Law, C. J., Abruzzo, M. W., Bassa, C. G., et al. 2017, ApJ, 850, 76
Lawrence, E., Vander Wiel, S., Law, C., Burke Spolaor, S., & Bower, G. C. 2017, AJ, 154, 117
Lingam, M., & Loeb, A. 2017, ApJL, 837, L23
Lorimer, D. R., Bailes, M., McLaughlin, M. A., Narkevic, D. J., & Crawford, F. 2007, Sci, 318, 777
MacMahon, D. H. E., Price, D. C., Lebofsky, M., et al. 2018, PASP, 130, 044502
Macquart, J.-P., & Johnston, S. 2015, MNRAS, 451, 3278
Marcote, B., Paragi, Z., Hessels, J. W. T., et al. 2017, ApJL, 834, L8
Masui, K., Lin, H.-H., Sievers, J., et al. 2015, Natur, 528, 523
Meyers, B. W., Tremblay, S. E., Bhat, N. D. R., et al. 2017, ApJ, 851, 20
Michilli, D., Seymour, A., Hessels, J. W. T., et al. 2018, Natur, 553, 182
Piro, A. L. 2016, ApJL, 824, L32
Price, D. C., Gajjar, V., Rosenthal, L., et al. 2018, arXiv:1802.04446
Scholz, P., Bogdanov, S., Hessels, J. W. T., et al. 2017, ApJ, 846, 80
Scholz, P., Spitler, L. G., Hessels, J. W. T., et al. 2016, ApJ, 833, 177
Spitler, L. G., Cordes, J. M., Hessels, J. W. T., et al. 2014, ApJ, 790, 101
Spitler, L. G., Herrmann, W., Bower, G. C., et al. 2018, arXiv:1807.03722
Spitler, L. G., Scholz, P., Hessels, J. W. T., et al. 2016, Natur, 531, 202
Tendulkar, S. P., Bassa, C. G., Cordes, J. M., et al. 2017, ApJL, 834, L7
Torne, P., Desvignes, G., Eatough, R. P., et al. 2017, MNRAS, 465, 242
van Straten, W., & Bailes, M. 2011, PASA, 28, 1
van Straten, W., Demorest, P., & Oslowski, S. 2012, AR&T, 9, 237
Worden, S. P., Drew, J., Siemion, A., et al. 2017, AcAau, 139, 98